Nanoscale

Accepted Manuscript

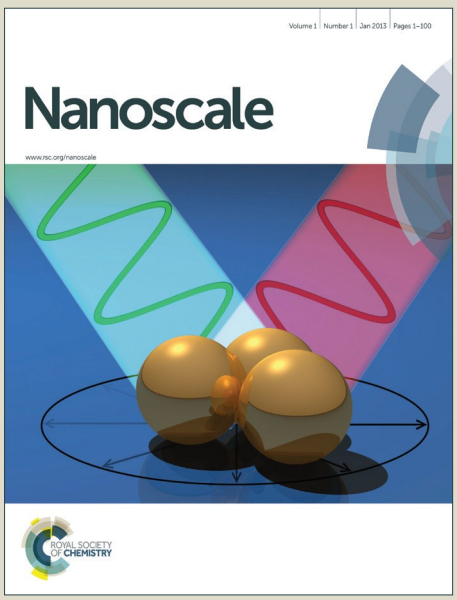

ROYAL SOCIETY OF CHEMISTRY

www.rsc.org/nanoscale

Nanoscale

PAPER

Spectral Triangulation: a 3D Method for Locating Single-Walled Carbon Nanotubes *in vivo*

Received 00th January 20xx,
Accepted 00th January 20xx

DOI: 10.1039/x0xx00000x

www.rsc.org/

Ching-Wei Lin,[a] Sergei M. Bachilo,[a] Michael Vu,[c] Kathleen M. Beckingham,[c] and R. Bruce Weisman[*,a,b]

Nanomaterials with luminescence in the short-wave infrared (SWIR) region are of special interest for biological research and medical diagnostics because of favorable tissue transparency and low autofluorescence backgrounds in that region. Single-walled carbon nanotubes (SWCNTs) show well-known sharp SWIR spectral signatures and therefore have the potential for noninvasive detection and imaging of cancer tumours, when linked to selective targeting agents such as antibodies. However, such applications face the challenge of sensitively detecting and localizing the source of SWIR emission from inside tissues. A new method, called spectral triangulation, is presented for three dimensional (3D) localization using sparse optical measurements made at the specimen surface. Structurally unsorted SWCNT samples emitting over a range of wavelengths are excited inside tissue phantoms by an LED matrix. The resulting SWIR emission is sampled at points on the surface by a scanning fibre optic probe leading to an InGaAs spectrometer or a spectrally filtered InGaAs avalanche photodiode detector. Because of water absorption, attenuation of the SWCNT fluorescence in tissues is strongly wavelength-dependent. We therefore gauge the SWCNT-probe distance by analysing differential changes in the measured SWCNT emission spectra. SWCNT fluorescence can be clearly detected through at least 20 mm of tissue phantom, and the 3D locations of embedded SWCNT test samples are found with sub-millimeter accuracy at depths up to 10 mm. Our method can also distinguish and locate two embedded SWCNT sources at distinct positions.

Introduction

The unique optical properties of single-walled carbon nanotubes (SWCNTs) suggest a number of intriguing applications in biological research and medical diagnostics.[1-3] SWCNTs are tubular nanoparticles composed of carbon atoms covalently bonded into various well defined crystalline structures. Each possible structure can be labelled by a pair of integers, (*n*,*m*), that specify its diameter, roll-up angle, metallicity, and (for semiconducting species) band gap. Semiconducting SWCNTs with diameters near 1 nm, such as those grown by the HiPco process, can fluoresce at specific short-wave infrared (SWIR or NIR-II) wavelengths from approximately 850 to 1600 nm when excited with red light.

Fluorescence imaging in biological tissues is greatly hampered by absorption, scattering, and autofluorescence backgrounds. Absorption of excitation and emission light passing through tissues decreases the detectable fluorescence intensity. Light scattering is also a severe problem for two reasons: it degrades image sharpness by spatially diffusing light emitted from a fluorescent centre (see Fig. S6), and it also increases absorption losses because the detected light can travel through indirect diffusional paths that are significantly longer than direct unscattered paths. Furthermore, autofluorescent emission from endogenous fluorophores in tissues gives diffuse backgrounds that can degrade image contrast or entirely mask weak signals. Scattering and autofluorescence generally decrease at longer wavelengths of excitation and emission, and the spectral window for minimal tissue absorption (between the haemoglobin and water maxima) lies in the SWIR,[4] matching the fluorescence wavelengths of many SWCNT species. The use of SWCNT fluorescent markers is therefore promising despite their limited emissive quantum yields.[5-7] Research on fluorescence detection and imaging of SWCNTs in biological environments began with cell cultures,[3, 8] insects,[9] and tissue specimens,[10, 11] and has recently been extended to *in vivo* studies.[12]

An important goal for *in vivo* imaging is the non-invasive diagnosis and monitoring of cancer through optical detection of tumour nodules.[13, 14] One strategy is to link fluorescent agents to antibodies that target cancer-specific cell markers.[15, 16] To avoid the fluorescence quenching that can result from covalent bonding to SWCNT sidewalls, Dai and co-workers developed a method for noncovalent conjugation of SWCNTs to phospholipid surfactants that are covalently bonded to

[a] *Department of Chemistry and the Smalley-Curl Institute, 6100 Main Street, Houston, TX 77005, USA*
[b] *Department of Materials Science and NanoEngineering, 6100 Main Street, Houston, TX 77005, USA*
[c] *Biosciences at Rice, Rice University, 6100 Main Street, Houston, TX 77005, USA.*
* Corresponding author. Email: weisman@rice.edu, Phone: +1 713 348 3709.
†Electronic Supplementary Information (ESI) available: Details concerning instrumental design, experimental procedures, related experiments, and triangulation computations, plus a video showing operation of the scanner. See DOI: 10.1039/x0xx00000x

antibodies.[12] By injecting SWCNTs into the bloodstream of small animals such as mice, two dimensional (2D) *in vivo* SWIR fluorescence images of vasculature could be obtained, sometimes at video rates.[6, 17-29] However, optical detection of cancer nodules located more than a few millimetres under the skin is very challenging because concentrations of emissive probes may be quite low and their emission is strongly attenuated passing through tissues. These factors may prevent the detection of SWCNT fluorescence even when backgrounds are very weak. Another limitation is that 2D images acquired from a single observation axis do not reveal the depths of emissive objects. There is thus a need for *in vivo* methods to detect SWIR fluorescent agents deeper inside tissues and to locate them in three dimensions.

We report here a novel spectral triangulation approach that is designed to noninvasively locate small tumours marked by SWCNT fluorescent immunoprobes. In this method, the subject is diffusely illuminated with visible light from an LED matrix and the resulting SWIR emission from nanotubes at the tumour site is sampled at a coarse grid of discrete positions on the skin, rather than being imaged by a SWIR-sensitive camera. At each sampled position, the fluorescence intensity is measured through two alternating SWIR spectral filters by a sensitive single-channel detector, a photon-counting InGaAs avalanche photodiode (APD). Because the two filtered spectral channels correspond to weak and strong optical absorption by water in tissues,[30] the ratio of their intensities can be interpreted with the help of an empirical calibration curve to deduce the distance between the sampling position and the emission source. By numerically analysing the full grid set of intensities, we can triangulate the three dimensional coordinates of the nanotube source with high precision and accuracy at depths in tissue phantoms to 10 mm. Our method can also be extended to recognise spatially extended emission sources and to detect without triangulation at depths beyond 20 mm.

RESULTS AND DISCUSSION

SWCNT-scanner design

Our SWCNT-scanner, described in detail in Materials and Methods, is designed to capture and analyse very weak signals from nanotubes inside tissues. A key feature is the use of an LED matrix for excitation. In clear optical media, lasers are more effective excitation sources than LEDs because their spatial coherence allows tight focusing. However, strong scattering in turbid media removes this advantage, and the LED matrix provides higher total optical power, good illumination uniformity at the specimen surface, and lower cost. We use a trans-illumination geometry, placing the LED matrix on the opposite side of the specimen from the detection probe. Compared to epi-illumination, this gives more uniform sensitivity through the specimen's depth, because regions far from the probe position receive more intense excitation. However, trans-illumination will not be effective for specimens more than a few centimetres thick. SWCNT fluorescence emerging at the surface is quite weak after passing through millimetres of highly scattering tissue. We therefore detect using a cooled InGaAs APD designed for photon counting. Although this single-channel configuration limits spectral resolution, it gives much greater sensitivity than is available from InGaAs-array modular spectrometers, even with spectral integration of their signals (Fig. S7).

In order to increase the optical efficiency, we collect fluorescence using an optical fibre positioned directly at the

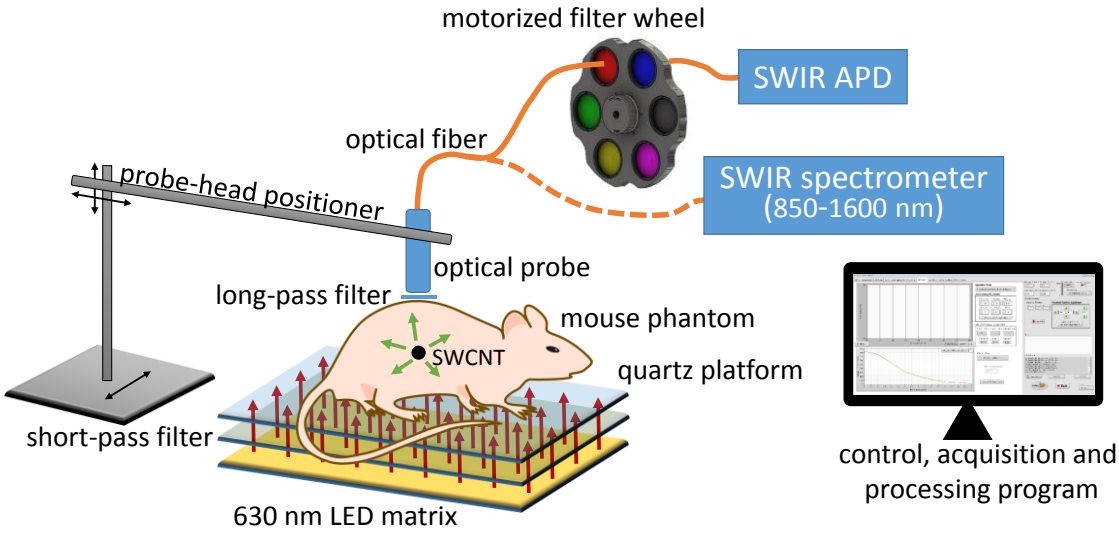

Fig. 1 Schematic diagram of the SWCNT optical scanner. Specimens such as mouse-shaped optical phantoms are placed on a transparent platform above a matrix of excitation LEDs. SWIR fluorescence emission from SWCNTs is sampled at the specimen top surface by an optical probe mounted on a three dimensional positioning system. Fluorescence passes through an optical fibre for detection either by a multichannel InGaAs spectrometer, or by an InGaAs avalanche photodiode behind a computer-controlled filter wheel. A computer running a custom LabVIEW program controls data acquisition and processing.

specimen surface, avoiding losses from surface reflections and chromatic aberration that a transfer lens would introduce. The optical fibre leads either to a multichannel InGaAs spectrometer to measure full SWCNT spectra during method development, or through a filter wheel to the APD for method implementation. This computer-controlled filter wheel passes SWIR fluorescence in two wavelength bands chosen to have distinct H_2O absorption coefficients.

Fig. 1 shows a schematic diagram of the scanner apparatus. Tissue phantoms shaped as rectangular sheets or mice were placed on the water-cooled fused silica specimen platform located over a short-pass filter and the excitation matrix containing 500 LEDs emitting near 630 nm. The optical probe was moved to the desired x- and y-coordinates and then lowered, stopping when its small mechanical switch sensed contact with the specimen surface. Light entering the optical probe fibre was long-pass filtered to remove scattered excitation light before transmission either to the SWIR spectrometer or to the filter wheel / APD detector. Although our system cannot generate images as well or quickly as SWIR camera-based devices, it does provide spectral information (using the spectrometer) or highly sensitive detection (using the APD). Irradiation of the specimen is minimized by switching on the LED matrix only during fluorescence acquisition. All instrument control, data acquisition, and data analysis are automated with custom LabVIEW software.

SWCNT spectra through tissue phantoms

Fig. 2 compares three spectra acquired from the instrument with no specimen in place, with a tissue phantom specimen free of SWCNTs, and with a tissue phantom containing unsorted SWCNTs. The first of these confirms a very low instrumental background above 900 nm. The second shows autofluorescence from the tissue phantom that is significant at shorter emission wavelengths, decreases markedly above 950 nm, and is negligible above 1150 nm. This observation is consistent with recent bio-imaging research focused on eliminating tissue background signals by using longer wavelength fluorophores.[24, 31] Comparison of the second and third traces in Fig. 2 suggests that spectral subtraction is an effective method to correct for autofluorescence backgrounds and deduce net spectra of SWCNTs inside tissue specimens. Preliminary data from a live mouse show autofluorescence backgrounds comparable to those from our tissue phantom.

We have used this correction method to measure fluorescence spectra from planar SWCNT samples through different depths of tissue phantoms. Fig. 3a shows these results for depths of 1 to 10 mm, with major peaks labelled by the corresponding (*n,m*) structures. As expected for light propagating through turbid media, the SWCNT emission is attenuated by both absorption and scattering.[32] To clarify the wavelength dependence of this attenuation, Fig. 3b shows semi-logarithmic plots of detected emission intensity *vs.* phantom thickness for the five labelled peaks representing the (6,5), (7,5), (7,6), (8,6), and (10,3) SWCNT species. It can be seen

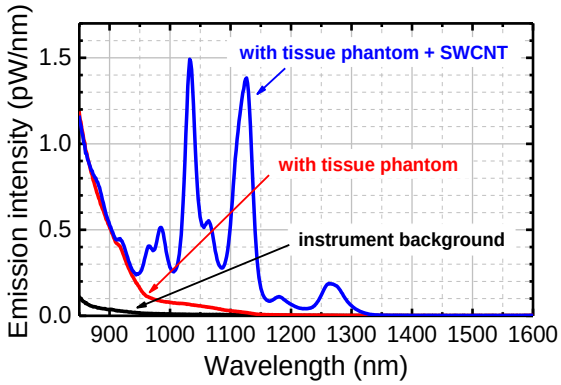

Fig. 2 SWIR spectra (as power entering the optical fibre probe) measured with the same parameters using the apparatus shown in Fig. 1. The lowest (black) curve shows the instrumental background with no specimen. The middle (red) curve shows signals (including instrumental background) measured from a 10 mm thick tissue phantom containing no SWCNTs. Autofluorescence is evident here below 1100 nm. The upper (blue) curve was measured from a tissue phantom containing a small embedded SWCNT sample.

that the attenuation for each peak is rather well described by a linear fit corresponding to a simple exponential relation

$$I(\lambda,d) = A_{\text{planar}}(\lambda)\,\mu(\lambda)\,e^{-\mu(\lambda)\,d}$$

where d is the emitter-to-probe distance, μ is the wavelength-dependent attenuation coefficient, and $A_{\text{planar}}(\lambda)$ is proportional to the source emission spectrum before attenuation by the medium.[33] In Fig. 3c we plot attenuation through 10 mm of tissue phantom as a function of wavelength and, for comparison, through the same thickness of water. The similarity in shape of the two traces indicates that attenuation in the tissue phantom at these wavelengths arises from water absorption enhanced by the longer effective photon path lengths from scattering.[30] Fig. 3d shows the same data inverted to give penetration depth *vs.* wavelength, or the thickness of tissue phantom that causes a factor of 10 attenuation. For a planar emission source, as used in this experiment, the penetration depth lies between 4 and 12 mm for SWIR wavelengths between 900 and 1350 nm. Our penetration depth spectrum is consistent with a prior report for human mucous tissue.[34]

We note that penetration depth depends on the source geometry, and a planar source gives the maximum values.[33] Our use of a large matrix of 630 nm LEDs provides a quasi-planar excitation geometry with a penetration depth we measure as ~9.1 mm (Fig. 3d). Detecting SWCNT emission sources of lower dimension (point or line shapes) will involve a steeper drop in detected signal with increasing source depth below the specimen surface than is suggested by Fig. 3b or 3c.

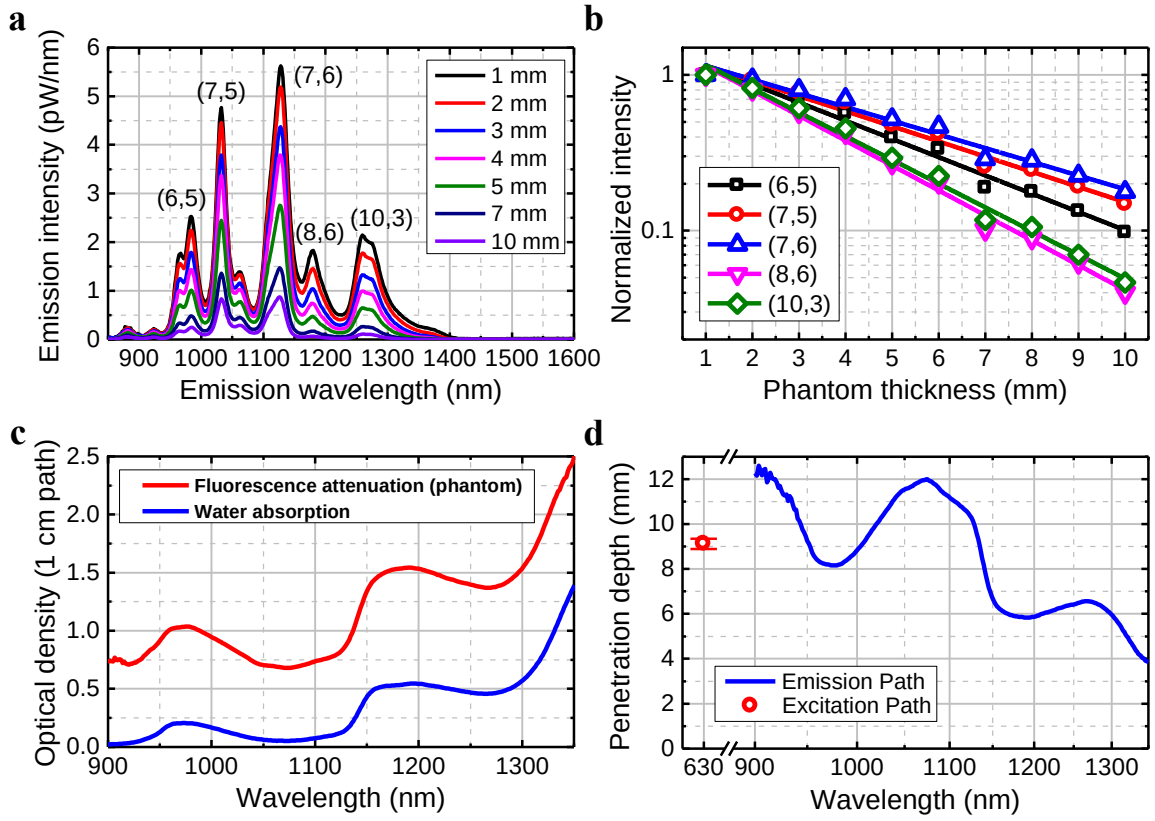

Fig. 3 Wavelength-dependent attenuation of fluorescence from a planar SWCNT emission source. (a) SWCNT fluorescence spectra measured through 1 to 10 mm thicknesses of tissue phantoms (as labelled). (b) Normalized fluorescence intensity *vs.* phantom thickness for the five (*n*,*m*) emission peaks marked in (a), with points in each data set fit to the exponential relation $I(\lambda,d) = A_{\text{planar}}(\lambda)\,\mu(\lambda)\,e^{-\mu(\lambda)\,d}$. (c) Fluorescence attenuation spectra in tissue phantom and in pure water shown as optical density through a 1 cm path length. (d) Fluorescence attenuation spectrum through tissue phantom shown as the 10% penetration depth. The penetration depth measured for the 630 nm excitation wavelength is shown by the red circle.

Spectral depth gauging

Our method of spectral triangulation is based on wavelength-dependent differences in SWCNT fluorescence attenuation arising from the water absorption spectrum intrinsic to tissues. This differs from the spectral triangulation reported by Yang *et al.*, in which the absorption spectrum of a contrast agent (indocyanine green) is used to profile the spatial distribution of the contrast agent in optical coherence tomography imaging.[35] Fig. 4a shows the SWCNT spectra of Fig. 3a normalized to the peak near 1120 nm. It can be seen that wavelengths longer than 1200 nm are attenuated much more strongly with tissue path length compared to those near 1120 nm. However, an obstacle to using this differential absorption effect for deducing the three dimensional positions of local SWCNT sources (e.g. in an antibody-targeted tumour) is the dependence of optical collection efficiency on angle θ between the source direction and the probe axis (Fig. 4b). We suppress this strong angular dependence (see Fig. S8 and S9) by mounting a thin Teflon scatter plate at the end of the collection fibre, as shown. During *in vivo* measurements, strong scattering by the skin (typical reduced scattering coefficient μ_s'=3 to 16 cm^{-1}, with anisotropy g = 0.9)[36] may play the role of our scatter plate. With the Teflon scatter plate in place, we measured fluorescence signals from a 1 μL SWCNT emission source that was sandwiched between two layers of tissue phantom. The bottom layer (between the SWCNTs and the LED excitation matrix) was 10 mm thick, while the top layer (between the SWCNTs and the detection probe) was varied from 1 to 9 mm, allowing us to obtain optical path lengths up to 20 mm by increasing the angle θ in Fig. 4b. For each thickness of the top layer, our APD detected emission signals through either a band pass filter centred at 1120 nm or a 1200 nm long pass filter. These two spectral segments are marked by the coloured rectangles in Fig. 4a and were chosen to select regions that have significant SWCNT emission and low autofluorescence, but very different amounts of absorption from water.

The results from these measurements are plotted in Fig. 4c, which shows the fluorescence attenuation from a sample containing ~34 ng of unsorted SWCNTs. The measured intensity decreases smoothly with path length but remains clearly detectable through at least 20 mm of tissue phantom. To our knowledge, this is the deepest reported detection of fluorescent markers inside tissues or tissue phantoms.[37] We also

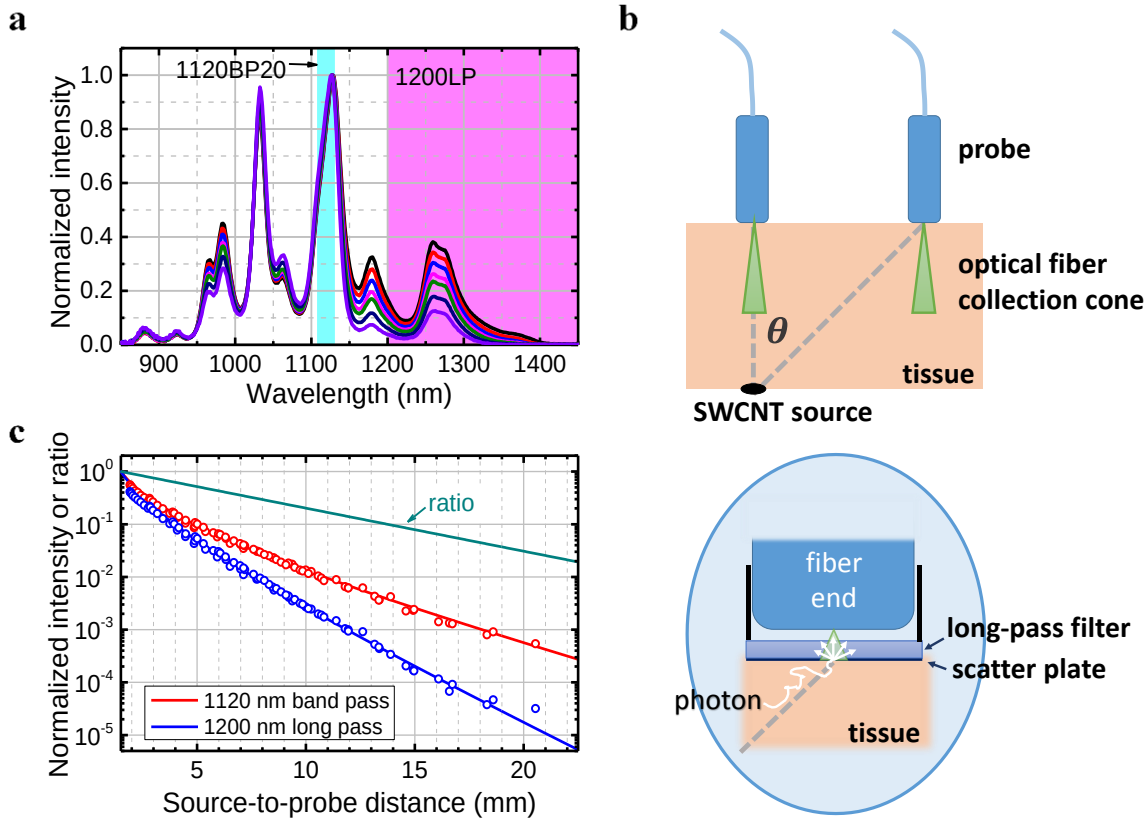

Fig. 4 Wavelength-dependent attenuation of fluorescence from SWCNT emission source through tissue phantoms. (a) Normalized fluorescence spectra from Fig. 3a, illustrating spectral shape changes with path length. The two shaded spectral regions are selected for APD acquisition by an 1120 nm band-pass filter and a 1200 nm long-pass filter. (b) Illustration of fluorescence collection geometry for two positions of the emission probe. For the position on the right, light travelling directly from the source falls outside the fibber's collection cone but is sampled by diffuse scattering in a thin Teflon scatter plate. (c) Normalized intensity from a small spherical SWCNT source measured in the two spectral bands vs. SWCNT-probe distance. The data were acquired by proving at various positions on the surfaces of tissue phantoms ranging in thickness from 1 to 10 mm. Solid lines show fits using the relation $I(\lambda,d) = A_{\text{spherical}}(\lambda)\,\mu^2(\lambda)\,e^{-\mu(\lambda)\,d}/d$. No dependence on angle θ was observed.

note that 20 mm gives sufficient range to probe internal organs of laboratory mice (see Fig. S9). Except at the shortest distances, the observed attenuation of SWCNT fluorescence with path length agrees with the following expression obtained from photon diffusion theory:[33]

$$I(\lambda,d) = \frac{A_{\text{spherical}}(\lambda)\,\mu^2(\lambda)\,e^{-\mu(\lambda)\,d}}{d}$$

Here, $A_{\text{spherical}}(\lambda)$ is related to the source intensity and the absorption coefficient and $\mu(\lambda)$ is the attenuation coefficient. We find empirical attenuation coefficients of 0.243 mm^{-1} and 0.432 mm^{-1} for the 1120 nm band-pass and 1200 nm long-pass signals, respectively. These are similar to the μ value of 0.26 mm^{-1} reported by Nishimura *et al.* for attenuation of 1300 nm light through human forearm tissue.[38] We also note that the isotropic scattering coefficient for 1% Intralipid tissue phantom was estimated to be ~0.85 mm^{-1} with an anisotropy factor g near 0.9. The absorption coefficient was estimated to be 0.12 mm^{-1} at 1200 nm, leading to an effective attenuation coefficient of 0.59 mm^{-1} (see Supplementary Information).[32, 34, 39]

SWCNT source triangulation

Using the results in Fig. 4c for calibration, one can deduce the location of a SWCNT emission source based on signals collected at three or more positions on the surface of the specimen. Fig. 5a illustrates the concept of this spectral triangulation. Suppose there is a localized SWCNT source fluorescing inside a tissue that gives fluorescence signals S_i measured at positions i on the specimen surface. For each S_i, the corresponding distance d_i to the source can be calculated from the intensity ratio in the two spectral bands, using the normalized ratio curve of Fig. 4c scaled by the ratio with no tissue present. Given three known measurement positions and their corresponding d_i values, one can geometrically compute a unique solution for the 3D coordinates of the SWCNT source.

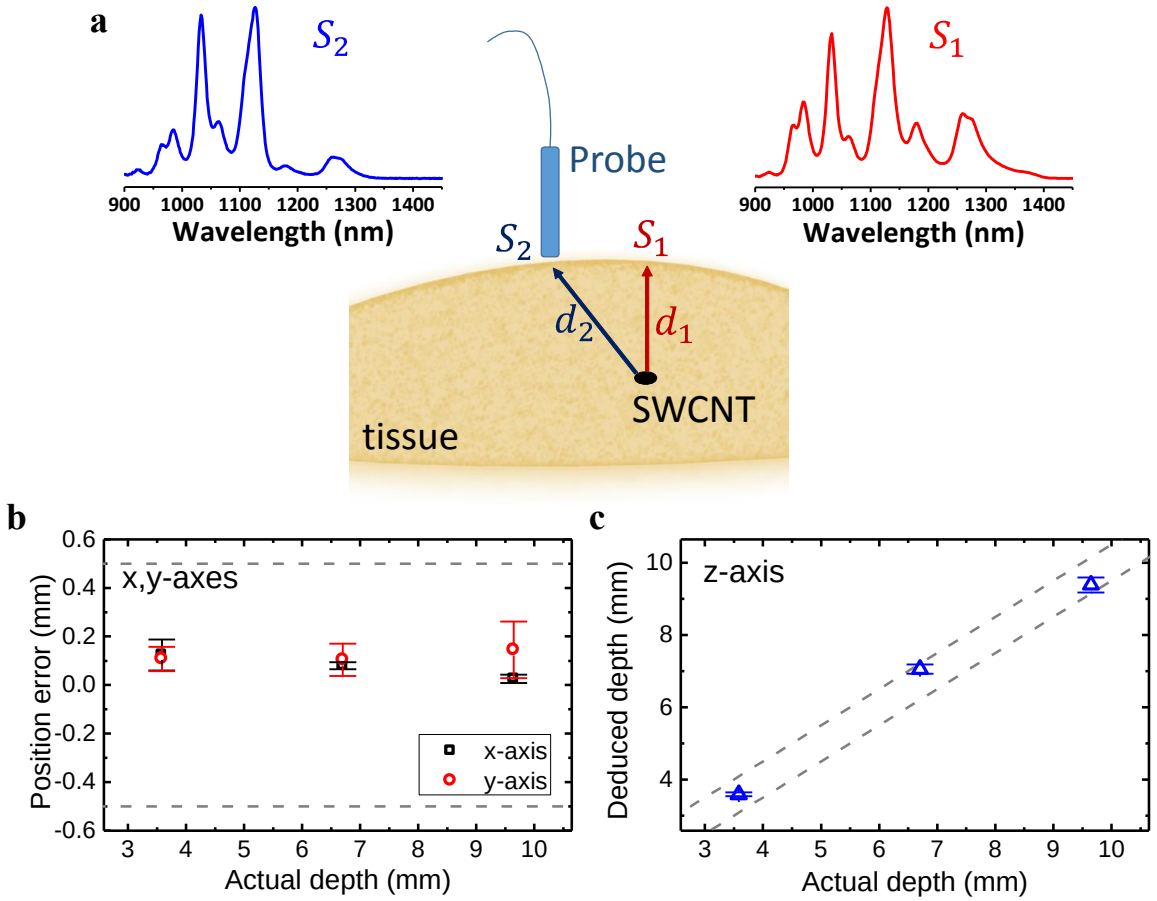

Fig. 5 Spectral triangulation scheme and results. (a) Measured spectral shapes depend on probe position, reflecting different average path lengths from source to probe through tissue. Analysis of spectral ratios from several probe positions gives coordinates of source. (b) Errors in the x- and y-coordinates deduced by spectral triangulation of an emission source at three different source depths. The separation between horizontal dashed lines indicates the diameter of the source, and error bars show standard deviations of replicate determinations. For each triangulation, twenty grid points were measured with 2 filters at each point and 2 s acquisitions, giving a total measurement time below 3 min including probe positioning. (c) Source depth coordinates deduced from spectral triangulation are plotted vs. actual depth. Dashed lines mark the boundaries of the source, and error bars show standard deviations.

In practice, we implement the triangulation calculation using a more general mathematical method that can give improved accuracy by analysing over-determined data sets with an arbitrary number of measurement positions and spectral bands (see Supplementary Information for details). To test our approach, we examined the precision and accuracy of locating a ~1 μL SWCNT source sandwiched between a 10 mm tissue phantom bottom layer and a top layer of tissue phantoms of three different thicknesses. For each top layer thickness, we measured signals at 20 grid points, accumulating for 2 s at each point for each spectral filter. Fig. 5b shows a plot of errors in the triangulated SWCNT source x and y coordinates *vs.* thickness of the top layer. Statistical uncertainties in the deduced coordinates (represented as error bars) tended to increase with depth of the source but were less than 0.12 mm, and the averaged deduced coordinates were accurate to approximately 0.1 mm, or only 10% of the source diameter. The source depths deduced by triangulation are plotted in Fig.

Table 1 Spectrally triangulated positions of the SWCNT source embedded in a mouse-shaped optical phantom.

	Position (mm)					
	x	x error	y	y error	z	z error
Deduced source coordinates	75.99	-0.27	74.50	-0.09	7.58	-0.28

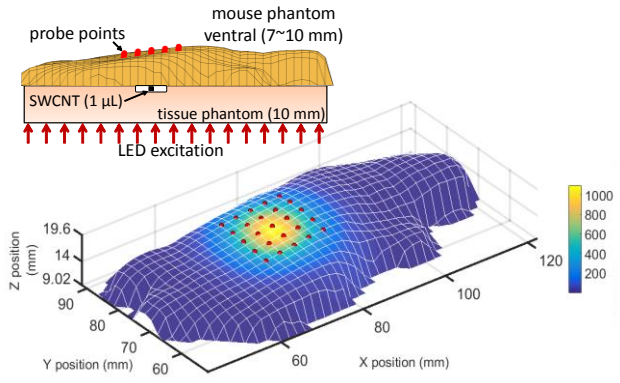

Fig. 6 Spectral triangulation of a localized SWCNT source in a mouse-shaped phantom. A side view of the setup is shown in the top left diagram. The SWCNT emission source was inserted between the lower surface of a mouse phantom and a 10 mm thick tissue phantom bottom plate. Data acquisition was performed with the probe at locations marked by red dots on the contour plot representing the mouse phantom ventral surface. Colours on the plot code for SWCNT fluorescence intensities predicted from the deduced source position.

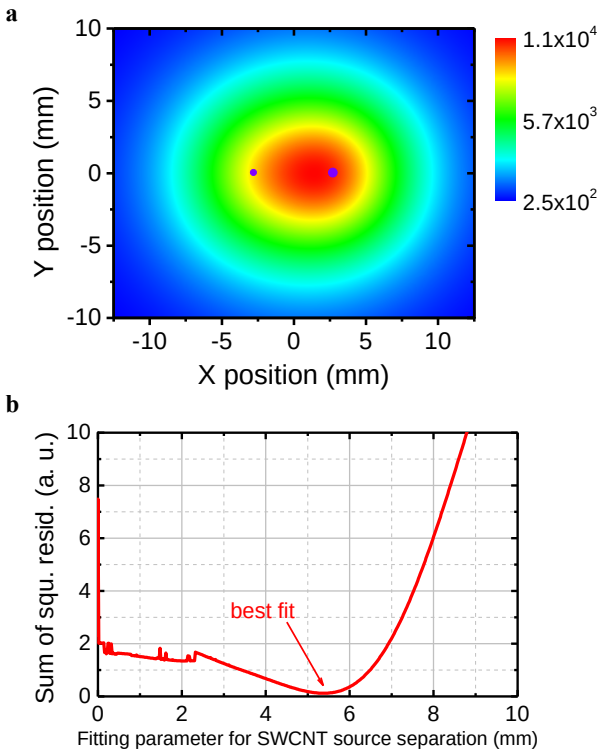

Fig. 7 Spectral triangulation of two SWCNT sources separated along the x-axis. (a) Slightly elongated contour plot of fluorescence intensities at the surface, as predicted from spectrally triangulated SWCNT source positions (purple dots). Dot diameters indicate relative fluorescence intensities of the sources. (b) Sum of squared residuals (SSR) in fits to measured set of intensities vs. the fitting parameter of SWCNT source separation. Other parameters including source y- and z-coordinates and intensities were floated during the fits. The minimum in SSR is found for a deduced source separation of 5.47 mm.

5c *vs.* actual depth, with dashed lines marking the dimension of the source. Although these deduced z-axis coordinates are somewhat less accurate than the x- and y-values, they show errors below 0.4 mm (less than half of the source diameter) even at a depth of 9.7 mm. This demonstrates the capability for accurate three-dimensional triangulation in highly scattering media based on pairs of spectral readings at only a few surface locations. In these tests, the entire spectral triangulation process including probe positioning, signal acquisition, and data processing was completed within 3 minutes.

We also tested spectral triangulation on a tissue phantom moulded in the shape of a mouse's ventral surface (see inset of Fig. 6). An emission source consisting of a capillary tube with ~1 μL of aqueous SWCNT suspension was placed on top of a 10 mm thick tissue phantom sheet and then covered with the mouse phantom, ventral side up. This positioned the SWCNT source 7 to 10 mm beneath the phantom's contoured surface. This "sandwich" specimen was excited from below with the LED matrix while emission was probed at a grid of 25 positions on the curved ventral surface. The acquisition time was again 2 s per point per filter. Fig. 6 shows the experimental geometry and the surface contour measured by the contact sensor. Red dots on the surface plot mark the probe positions used for data acquisition and the surface colours show SWIR intensities simulated from the analysis results. As displayed in Table 1, spectral triangulation revealed the position of the embedded emission source to an accuracy better than 0.3 mm in all three axes.

Localization with multiple emission sources

In practical applications of SWCNT-labelled antibodies for

Table 2 Spectrally triangulated position errors and standard deviations for two SWCNT sources embedded in a 15 mm thick tissue phantom.

SWCNT source	Depth (mm)	Source intensity (counts/s)	Position errors (mm)					
			Δx	Δx stdev	Δy	Δy stdev	Δ depth	Δ depth stdev
Left	6.33	141,400	-0.037	0.002	0.003	-0.002	0.004	0.002
Right	5.91	104,700	-0.068	-0.034	0.001	-0.002	0.015	0.013

non-invasive diagnosis of cancer nodules, one must be able to distinguish distinct emission sources arising from multiple tumour sites or accumulations of immunoprobes in non-targeted organs such as the liver. As a first step toward this goal, we have tested our method with a pair of localized SWCNT emission sources, 1.0 and 1.4 μL in volume and approximately 6 mm deep inside a 15 mm thick tissue phantom. The two sources were separated by 5.51 mm along the x-axis and had slightly different y and z coordinates. We acquired fluorescence data from a grid of 35 surface points and then performed triangulation calculations assuming the presence of two localized emission sources, using a variable parameter for the separation between them. Fit quality was assessed from the sum of squared residuals (SSR) between measured and simulated emission data optimized at each value of the separation parameter. Fig. 7b shows that the SSR reaches a distinct minimum for a separation parameter of 5.47 mm, indicating that the spectral triangulation analysis clearly deduced the presence of two emission centres and found their separation to an accuracy of 0.04 mm. This was achieved even though the fluorescence profile at the specimen surface has a single maximum and only slight elongation in shape, as shown in Fig. 7a by the colour-mapped surface contour reconstructed from the triangulated solution. Here, the purple dots mark the deduced source locations, with the dot diameters proportional to emission intensities. Table 2 shows errors and uncertainties in the deduced three-dimensional coordinates of the two emission sources. It can be seen these average errors are generally less than 0.1 mm, or only a small fraction of the source dimensions. Of course, accurate determinations of complex emission sources require photometric data of high enough quality to allow weak minima in curves such as Fig. 7b to be clearly discerned. Feasibility will vary with the separation between emission centres, their depths inside the tissue, the concentration of SWCNT emitters in the sources, the excitation intensity, the locations and number of probe positions, the data acquisition time per position, and the detector noise level. When analysing the emission data, it is also necessary to find best fits that are global rather than local.

Given the availability of high quality data, our method could be generalized to systems with unknown numbers of emission centres. For this, the triangulation model would initially fit the data set assuming a large number of centres. If the actual number is smaller, then some of the deduced source intensities will be found to be negligible compared to the others. Those can then be omitted from subsequent rounds of fitting until the minimum set of sources needed to adequately fit the data has been determined. We verified that this approach is successful for the simplest case: applying a two-source model to fit single source data. The analysis initially deduced one intense centre very near the correct position and a second separated centre having an intensity 25 times lower. After the weak apparent centre was neglected, re-triangulation with the single-source model accurately found the actual emission centre.

CONCLUSIONS

We have developed a novel approach to detect and three-dimensionally locate very weak SWCNT emission sources in turbid media such as biological tissues. The system is based on sensitive intensity measurements made at sparse discrete positions on the specimen surface. At each probed position, emission is measured in two complementary spectral ranges that have different attenuation coefficients arising from water in tissues. With the aid of empirical calibration data, the ratio of those measured intensities reveals distance from probe position to the emission source. Triangulation calculations using data from several probe positions then give emission coordinates with sub-millimetre accuracy.

This method has been demonstrated using tissue phantoms mimicking laboratory mice with embedded single and dual SWCNT emission sources. We excited specimens with a large LED matrix and detected SWCNT emission with a sensitive InGaAs avalanche photodiode. Accurate triangulation was achieved at depths up to 10 mm, and signals could be detected through at least 20 mm of tissue phantom. It was also possible to deduce the separation between dual embedded sources.

Practical *in vivo* applications of our method in animal studies will require further refinement. One issue is optical nonuniformities in real tissues that may cause inconsistent estimates of emission source locations when computed from different probe positions. This might be addressed by enhancing the grid of probe positions and/or by more elaborate calibration procedures, possibly including attempts to adjust attenuation coefficients for local differences in water content.[23, 30, 40-44] Another refinement might be the use of structurally enriched SWCNT samples, containing for example the (9,4) and (8,7) species. These could both be efficiently excited at 730 nm, allowing somewhat improved penetration of the excitation light. In addition, their distinct emissions near 1110 and 1270 nm would have well-defined attenuation coefficients and would avoid the 1200 nm absorption band of lipids and collagen. The use of sorted SWCNT samples may also allow compensation for autofluorescence backgrounds. If the SWCNT emission occurs only in narrow spectral range, signals from an adjacent range could be used for background subtraction. Finally, we note that trans-illumination is suitable only for exciting relatively thin specimens, so a more direct excitation path will be needed for clinical applications. We view the apparatus and method described here as complementary to camera-based SWIR *in vivo* imaging approaches. It offers advantages in terms of sensitivity, equipment cost, depth range, and depth measurement, but requires longer acquisition times and cannot capture detailed images. In the future, it may be possible to combine some capabilities of the two approaches by pixel-level processing of spectrally filtered camera data to obtain depth-resolved SWIR images. We hope that spectral triangulation will prove a useful tool for enhancing the value of SWCNT-based immunoprobes in biomedical research.

MATERIALS AND METHODS

SWCNT samples and tissue phantoms

SWCNTs used in this work were grown in the Rice University HiPco reactor (batch 195.1). A dispersion was prepared by mixing raw SWCNTs with a 0.5% (w/v) solution of sodium deoxycholate (DOC) in HPLC-grade water at a ratio of 0.5 mg SWNCTs per mL of solution and then applying 10 min of active tip ultrasonication at a power level of ~7 W. To remove aggregates, the resulting dispersion was ultracentrifuged at 25 °C for 4 h at 50,000 rpm (268,000g maximum, Beckman Coulter Optima Max), after which the supernatant was extracted and stored. Absorption and fluorescence spectra of this material are shown in Fig. S5. The SWCNT mass concentration was estimated as ~34 μg/mL using a base-10 mass extinction coefficient for unsorted HiPco dispersions of 0.043 $(mg/L)^{-1}$ cm^{-1} at 763 nm.[45] A 1 μL sample therefore contains ~34 ng of SWCNT material, or on the order of 10^{10} nanotubes.

We prepared a quasi-planar emission source used for measurements of spectra through tissue phantoms by injecting the SWCNT solution into a 15 x 15 x 0.05 mm channel on a fused silica slide. An emission source used to mimic small spherical nodules was made by injecting 1 μL of the SWCNT solution into a 1 mm ID fused silica capillary tube and then sealing it with epoxy glue.

We prepared tissue optical phantoms from a standard mixture of agar, Intralipid, and haemoglobin (see Supplementary Information). These were cast in the shape of rectangular plates using custom-fabricated aluminium moulds with defined thicknesses between 1 and 10 mm. The actual final thickness of each tissue phantom plate was measured using the contact sensor on the computer-positioned optical probe. To form mouse-shaped tissue phantoms, we used a silicone rubber mould that was custom-formed from the carcass of a nude laboratory mouse lying on its ventral surface (see Supplementary Information). Phantom mice were made by filling the mould with the same material used to make the tissue phantom plates.

SWCNT scanner

Our lens-free SWCNT-scanner contains the following components: a specimen platform with illuminator, an optical probe with contact sensor, a probe positioner, a SWIR spectrometer, and a SWIR single photon counter (SPC) with motorized filter wheel. Specimens are trans-illuminated to excite internal SWCNTs with a 50 × 50 mm LED matrix mounted under the specimen platform. This matrix contains 500 LEDs (20 × 25), each with maximum electrical input of 1 W and a peak emission wavelength of 630 nm (spectrum shown in Fig. S4). It can generate light intensities at the specimen of up to ~500 mW/cm^2 with ~230 W of electrical input. Power to the matrix is switched by a computer-generated TTL signal through a Darlington transistor. Above the LED matrix is a 4 mm thick Schott KG5 filter that blocks lamp emission in the SWIR region. The excitation source, filter, and specimen support plate are cooled by circulating water (see Supplementary Information). The probe, which consists of a custom touch-sensing electrical switch attached to a step-index optical fibre with a 400 μm, low-OH core, detects contact with the specimen surface and collects SWCNT emission for analysis by the detectors. An 800 nm long-pass dielectric filter mounted onto the end of the fibre prevents entry of stray excitation light, and a thin Teflon scatter film on the filter greatly reduces the angular dependence of collection efficiency. We control the position of the probe assembly by mounting it in place of the print head holder on a modified commercial 3D printer (Printrbot Simple Metal), which provides lateral resolution of 0.1 mm and vertical resolution of 0.01 mm. The other end of the optical fibre is attached either to a SWIR spectrometer with a 512-channel InGaAs array, or a single-channel InGaAs avalanche photodiode (APD). The spectrometer (B&WTek model Sol 1.7, 850-1600 nm, cooled to -15 °C) was calibrated for wavelength-dependent absolute sensitivity and contained an internal RG-830 long-pass filter. Acquisition times ranged from 0.2 to 25 s depending on signal intensity, and we sometimes averaged multiple acquisitions to improve signal-to-noise ratios. When detecting with the single-channel APD (ID Quantique model ID220, 600 s^{-1} dark count, --50 °C), collected light was first passed through a motorized filter wheel containing 1120 nm band-pass and 1200 nm long-pass filters. More detailed descriptions of the components are provided in Supplementary Information.

Spectral triangulation procedure

Spectral triangulation fluorescence data were measured with an average excitation intensity of ~250 mW/cm^2. We acquired SWCNT fluorescence at 20 to 35 positions on an x-y grid with the probe lowered to make contact with the specimen surface at each position. Then signals were recorded with the APD detector for 2 s through each of the two spectral filters. After correction for dark counts, the set of signals was analysed with the aid of attenuation coefficients (Fig. 4c) to deduce coordinates and intensities of the emission source(s). In this analysis, described in Supplementary Information, we minimized the sum of squared residuals (SSR) between experimental and modelled signals using the Simplex method.

Acknowledgements

This research was supported by grants from the National Science Foundation (CHE-1409698), the Welch Foundation (C-0807), the National Institutes of Health (R21CA171923), and the John S. Dunn Foundation Collaborative Research Award Program.

Notes and references

1. S. M. Bachilo, M. S. Strano, C. Kittrell, R. H. Hauge, R. E. Smalley and R. B. Weisman, *Science*, 2002, **298**, 2361-2366.

2. M. J. O'Connell, S. M. Bachilo, C. B. Huffman, V. C. Moore, M. S. Strano, E. H. Haroz, K. L. Rialon, P. J. Boul, W. H. Noon, C. Kittrell, J. P. Ma, R. H. Hauge, R. B. Weisman and R. E. Smalley, *Science*, 2002, **297**, 593-596.
3. P. Cherukuri, S. M. Bachilo, S. H. Litovsky and R. B. Weisman, *J. Am. Chem. Soc.*, 2004, **126**, 15638-15639.
4. A. M. Smith, M. C. Mancini and S. Nie, *Nat. Nanotechnol.*, 2009, **4**, 710-711.
5. T. Hertel, S. Himmelein, T. Ackermann, D. Stich and J. Crochet, *ACS Nano*, 2010, **4**, 7161-7168.
6. K. Welsher, S. P. Sherlock and H. Dai, *Proc. Natl. Acad. Sci. U. S. A.*, 2011, **108**, 8943-8948.
7. J. Crochet, M. Clemens and T. Hertel, *J. Am. Chem. Soc.*, 2007, **129**, 8058-8059.
8. D. Roxbury, P. V. Jena, Y. Shamay, C. P. Horoszko and D. A. Heller, *ACS Nano*, 2016, **10**, 499-506.
9. T. K. Leeuw, R. M. Reith, R. A. Simonette, M. E. Harden, P. Cherukuri, D. A. Tsyboulski, K. M. Beckingham and R. B. Weisman, *Nano Lett.*, 2007, **7**, 2650-2654.
10. D. Roxbury, P. V. Jena, R. M. Williams, B. Enyedi, P. Niethammer, S. Marcet, M. Verhaegen, S. Blais-Ouellette and D. A. Heller, *Sci. Rep.*, 2015, **5**, 14167.
11. P. Cherukuri, C. J. Gannon, T. K. Leeuw, H. K. Schmidt, R. E. Smalley, S. A. Curley and R. B. Weisman, *Proc. Natl. Acad. Sci. U. S. A.*, 2006, **103**, 18882-18886.
12. G. S. Hong, S. O. Diao, A. L. Antaris and H. J. Dai, *Chem. Rev.*, 2015, **115**, 10816-10906.
13. Y. Ardeshirpour, V. Chernomordik, J. Capala, M. Hassan, R. Zielinsky, G. Griffiths, S. Achilefu, P. Smith and A. Gandjbakhche, *Technol. Cancer Res. Treat.*, 2011, **10**, 549-560.
14. X. Y. Chen, P. S. Conti and R. A. Moats, *Cancer Res.*, 2004, **64**, 8009-8014.
15. X. H. Gao, Y. Y. Cui, R. M. Levenson, L. W. K. Chung and S. M. Nie, *Nat. Biotechnol.*, 2004, **22**, 969-976.
16. X. Qian, X.-H. Peng, D. O. Ansari, Q. Yin-Goen, G. Z. Chen, D. M. Shin, L. Yang, A. N. Young, M. D. Wang and S. Nie, *Nat. Biotechnol.*, 2008, **26**, 83-90.
17. Z. Liu, S. Tabakman, K. Welsher and H. Dai, *Nano Res.*, 2009, **2**, 85-120.
18. K. Welsher, Z. Liu, S. P. Sherlock, J. T. Robinson, Z. Chen, D. Daranciang and H. Dai, *Nat. Nanotechnol.*, 2009, **4**, 773-780.
19. S. Diao, G. Hong, J. T. Robinson, L. Jiao, A. L. Antaris, J. Z. Wu, C. L. Choi and H. Dai, *J. Am. Chem. Soc.*, 2012, **134**, 16971-16974.
20. G. Hong, J. C. Lee, J. T. Robinson, U. Raaz, L. Xie, N. F. Huang, J. P. Cooke and H. Dai, *Nat. Med.*, 2012, **18**, 1841-1848.
21. J. T. Robinson, G. Hong, Y. Liang, B. Zhang, O. K. Yaghi and H. Dai, *J. Am. Chem. Soc.*, 2012, **134**, 10664-10669.
22. A. L. Antaris, J. T. Robinson, O. K. Yaghi, G. Hong, S. Diao, R. Luong and H. Dai, *ACS Nano*, 2013, **7**, 3644-3652.
23. G. Hong, S. Diao, J. Chang, A. L. Antaris, C. Chen, B. Zhang, S. Zhao, D. N. Atochin, P. L. Huang, K. I. Andreasson, C. J. Kuo and H. Dai, *Nat. Photonics*, 2014, **8**, 723-730.
24. S. Diao, G. S. Hong, A. L. Antaris, J. L. Blackburn, K. Cheng, Z. Cheng and H. J. Dai, *Nano Res.*, 2015, **8**, 3027-3034.
25. S. Diao, J. L. Blackburn, G. Hong, A. L. Antaris, J. Chang, J. Z. Wu, B. Zhang, K. Cheng, C. J. Kuo and H. Dai, *Angew. Chem. Int. Ed.*, 2015, **54**, 14758-14762.
26. H. J. Yi, D. Ghosh, M. H. Ham, J. F. Qi, P. W. Barone, M. S. Strano and A. M. Belcher, *Nano Lett.*, 2012, **12**, 1176-1183.
27. C. Liang, S. Diao, C. Wang, H. Gong, T. Liu, G. Hong, X. Shi, H. Dai and Z. Liu, *Adv. Mater.*, 2014, **26**, 5646-5652.
28. Z. Liu, J. T. Robinson, S. M. Tabakman, K. Yang and H. Dai, *Mater. Today*, 2011, **14**, 316-323.
29. J. T. Robinson, K. Welsher, S. M. Tabakman, S. P. Sherlock, H. Wang, R. Luong and H. Dai, *Nano Res.*, 2010, **3**, 779-793.
30. R. H. Wilson, K. P. Nadeau, F. B. Jaworski, B. J. Tromberg and A. J. Durkin, *J. Biomed. Opt.*, 2015, **20**, 030901.
31. I. Villa, A. Vedda, I. X. Cantarelli, M. Pedroni, F. Piccinelli, M. Bettinelli, A. Speghini, M. Quintanilla, F. Vetrone, U. Rocha, C. Jacinto, E. Carrasco, F. S. Rodriguez, A. Juarranz, B. del Rosal, D. H. Ortgies, P. H. Gonzalez, J. G. Sole and D. J. Garcia, *Nano Res.*, 2015, **8**, 649-665.
32. T. Vo-Dinh, ed., *Biomedical Photonics Handbook*, CRC Press, Boca Raton, FL, 2003.
33. S. L. Jacques, *Photochem. Photobiol.*, 1998, **67**, 23-32.
34. A. N. Bashkatov, E. A. Genina, V. I. Kochubey and V. V. Tuchin, *J. Phys. D: Appl. Phys.*, 2005, **38**, 2543-2555.
35. C. H. Yang, L. E. L. McGuckin, J. D. Simon, M. A. Choma, B. E. Applegate and J. A. Izatt, *Opt. Lett.*, 2004, **29**, 2016-2018.
36. T. L. Troy and S. N. Thennadil, *J. Biomed. Opt.*, 2001, **6**, 167-176.
37. D. Ghosh, A. F. Bagley, Y. J. Na, M. J. Birrer, S. N. Bhatia and A. M. Belcher, *Proc. Natl. Acad. Sci. U. S. A.*, 2014, **111**, 13948-13953.
38. G. Nishimura, I. Kida and M. Tamura, *Phys. Med. Biol.*, 2006, **51**, 2997-3011.
39. L. H. Kou, D. Labrie and P. Chylek, *Appl. Opt.*, 1993, **32**, 3531-3540.
40. R. B. Schulz, A. Ale, A. Sarantopoulos, M. Freyer, E. Soehngen, M. Zientkowska and V. Ntziachristos, *IEEE Trans. Med. Imaging*, 2010, **29**, 465-473.
41. Q. Q. Fang, S. A. Carp, J. Selb, G. Boverman, Q. Zhang, D. B. Kopans, R. H. Moore, E. L. Miller, D. H. Brooks and D. A. Boas, *IEEE Trans. Med. Imaging*, 2009, **28**, 30-42.
42. B. Brooksby, B. W. Pogue, S. D. Jiang, H. Dehghani, S. Srinivasan, C. Kogel, T. D. Tosteson, J. Weaver, S. P. Poplack and K. D. Paulsen, *Proc. Natl. Acad. Sci. U. S. A.*, 2006, **103**, 8828-8833.
43. V. Ntziachristos, A. G. Yodh, M. Schnall and B. Chance, *Proc. Natl. Acad. Sci. U. S. A.*, 2000, **97**, 2767-2772.
44. V. Ntziachristos, *Nat. Meth.*, 2010, **7**, 603-614.
45. V. C. Moore, Ph.D. Ph.D. Thesis, Rice University, 2005.